

Point-Pattern Matching Technique for Local Structural Analysis in Condensed Matter

Arash D. Banadaki and Srikanth Patala*

*Department of Materials Science and Engineering,
North Carolina State University, Raleigh, NC*

Jason J. Maldonis and Paul M. Voyles

*Department of Materials Science and Engineering,
University of Wisconsin-Madison, Madison, WI*

Abstract

The local arrangement of atoms is one of the most important predictors of mechanical and functional properties of materials. However, algorithms for identifying the geometrical arrangements of atoms in complex materials systems are lacking. To address this challenge, we present a point-pattern matching algorithm that can detect instances of a template structure in a given set of atom coordinates. To our knowledge this is the first geometrical comparison technique for atomistic configurations with very different number of atoms, and when the optimal rotations and translations required to align the configurations are unknown. The pattern matching algorithm can be combined with an appropriate set of metrics to quantify the similarity or dissimilarity between configurations of atoms. We demonstrate the unique capabilities of the point-pattern matching algorithm using two examples where the automated analysis of local atomistic structure can help advance the understanding of structure-property relationships in material science: (a) identifying local three-dimensional polyhedral units along interfacial defects, and (b) the analysis of quasi-icosahedral topologies in the atomistic structure of metallic glasses. We anticipate that the pattern matching algorithm will be applicable in the analysis of atomistic structures in broad areas of condensed matter systems, including biological molecules, polymers and disordered metallic systems. An online implementation of the algorithm is provided via the open source code hosted on GitHub (<https://github.com/spatala/ppm3d>).

I. INTRODUCTION

In materials science, structure is typically described using atoms as fundamental units and the properties are inferred through the spatial arrangements of atoms relative to each other. The length scales involved may vary from short-range (near-neighbors) and medium-range to long-range depending on the structure and properties of interest. Even when the analysis of structure at larger length scales is necessary, the characterization of the relative arrangement of atoms in the first coordination shell has proven to be of great importance^{1,2}. For perfect crystals, the machinery of crystallography provides a complete, succinct, and extremely powerful description of the positions of all the atoms, but there is no parallel description for aperiodic structures, including defects in crystalline materials such as grain boundaries and the structure of glasses. In such cases, we do not have a general description (or quantification) of even the local structure. A parallel problem arises in atomistic simulations. In this case, the position of every atom is known, often as a function of time, yielding a great deal of data, but leaving us with a need for a general, automated analysis approach to develop abstract structural descriptions from this detailed data.

Some of the most commonly utilized structural analysis methods for atomistic simulations include: centro-symmetry parameter, bond-order analysis, common-neighbor analysis, bond angle analysis, and Voronoi-cell topology. The first four techniques involve computing for each atom in the system a scalar quantity, an order-parameter, which depends on the spatial location of the atom's neighbors. Voronoi-cell topology uses a topological descriptor, the Voronoi index or the p -vector^{3,4}, instead of a scalar calculated from spatial locations as the order parameter. These quantities are invariant to rigid body rotations and translations of the local atomic environment. While these simplified order parameters have been invaluable in the analysis of the distributions of different types of defects and their evolution during atomistic simulations, they suffer from issues involved with degeneracies and large sensitivity to small perturbations. The degeneracies arise as the order parameters are simply projections of a high-dimensional atomistic configuration space to a single scalar value, as described in Lazar *et al.*² For example, the centro-symmetry parameter exhibits similar values for either an atom that is present along a defect (such as a dislocation or a grain boundary) or one that is in a bulk single crystal at moderately high temperatures (*e.g.* $0.5 T_m$).

The issue of high sensitivity to small perturbations is evident when using the Voronoi

cell topology as a descriptor. For any topological descriptor, there will exist atomic configurations where a small change in the position of one of the atoms will change the topology of the descriptor². Another limitation of the structure classifiers is that all the quantities measured are per-atom descriptors. That is, each atom gets a scalar value or a topological index. However, in complex systems, *e.g.* along defects in crystalline materials (such as dislocations and grain boundaries) or in quantifying medium-range order in glasses, it is the geometrical patterns and the connectivity of a sub-set of atoms in the system that are of interest. In these systems there is no clear notion of a *center-atom* around which the structure is quantified. Therefore, traditional structure quantification techniques are not capable of discerning the connectivity between atoms in complex, disordered material systems.

In order to address these challenges, we propose a point-pattern matching technique for direct characterization of local atomic structures. Point-pattern matching (PPM) is a fundamental problem in pattern recognition with applications in a broad range of fields including computer vision^{5–10}, computational chemistry^{11,12}, astronomy^{13,14} and computational biology^{15,16}. More specifically, PPM methods are *feature detection algorithms* that can identify specific features in an environment. PPM techniques use a metric to quantify the similarity (or dissimilarity) between atomic environments, as described in section II. This allows for a quantitative measure of how structure changes, for example, as temperature is increased or when the crystallographic nature of the defect is varied (see section III A). PPM algorithms can also account for small perturbations that arise due to thermal vibrations, making them ideal for the analysis of local atomic structure in disordered material systems. Most notably, with a suitable metric, unsupervised machine learning algorithms, such as clustering, can be used to analyze the underlying geometries in the material¹⁷.

In the following sections, we first introduce the PPM algorithm with a simple two-dimensional example. Then, we present two material science problems illustrating the unique capabilities of the PPM algorithm for analyzing structures in atomistic models. The first is the identification of polyhedral motifs in the disordered regions of a metallic grain boundaries (section III A). In this example, the objective is to identify model polyhedral units¹⁸ along the atomic structure of grain boundaries (GBs). The polyhedral units are much smaller than the GB structure, so this application takes advantage of the capability of PPM to match sets with very different number of atoms. In the second example (section III B), we use the PPM technique to identify clusters with icosahedral geometry in a Zr-Cu-Al metallic glass

for comparison to clusters with icosahedral topology as identified by their Voronoi indices.

II. METHODOLOGY

In the terminology used in image-processing, atoms are referred to as points and the sets of atoms being compared are point-sets. To quantify the (dis)similarity between two point-sets, we compare a set of m points (the *model*, \mathbf{M} , also known as the *template*) to a set of n points (the *target*, \mathbf{T}). The positions of the points in the model, \mathbf{M} , and in the target, \mathbf{T} , are given by the set of vectors $\mathbf{R}^{\mathbf{M}} = \{\mathbf{r}_1^M, \mathbf{r}_2^M, \dots, \mathbf{r}_m^M\}$ and $\mathbf{R}^{\mathbf{T}} = \{\mathbf{r}_1^T, \mathbf{r}_2^T, \dots, \mathbf{r}_n^T\}$, respectively. The objective is to find a set of m points in the target that are most similar to the configuration of points in the model set. That is, we wish to find a one-to-one mapping between the atoms in the model and the target, a rotation matrix, and a translation vector that best overlaps the points in the model with those in the target set.

In the general problem, the number of points n in the target is greater than those in the model, *i.e.* $n \geq m$. A brute-force technique requires picking $\binom{m}{n}$ sub-sets of m points in the target, and finding the correspondence requires another $m!$ comparisons. Hence, the algorithm, in the worst case, has the complexity of $O(n!/(n-m)!)$, which is computationally unfeasible for large values of n and m . A wide variety of approaches have been proposed in the fields of image processing^{19,20} and computational chemistry^{21–30} to render this general problem computationally feasible.

In condensed-matter systems, the goal is to compare and characterize molecular structures. When the number of atoms in the model and the target are equal (*i.e.* $n = m$), the similarity (or dissimilarity) between point-sets is quantified using the root-mean-square-distance (RMSD) parameter, defined as²³:

$$\text{RMSD} = \frac{1}{\sqrt{m}} \min_{f, U, \mathbf{t}} \sum_{i=1}^m d(U\mathbf{r}_i^M + \mathbf{t}, \mathbf{r}_{f(i)}^T), \quad (1)$$

where $d(\cdot, \cdot)$ is the Euclidean distance metric. The minimization is over all possible permutations of indices, given by the function f , rotations of the model, U , and relative translations \mathbf{t} . The permutation function f maps the indices of the points in the model to those in the target. For example, if $f(i^m) = j^t$, then the i^{th} index in the model is mapped to the j^{th} index in the target (the same information may also be represented using a $m \times m$

permutation matrix). We denote the operations f , U and \mathbf{t} that minimize RMSD as \hat{f} , \hat{U} , and $\hat{\mathbf{t}}$, respectively. The RMSD defined as such obeys the three properties of a metric³¹: (a) the coincidence axiom, (b) symmetry, and (c) the triangle inequality.

If the minimizing rotations and translations, \hat{U} , and $\hat{\mathbf{t}}$, are known *a priori*, the permutation matrix can be obtained using the Hungarian algorithm³², which has the algorithmic complexity of $O(m^3)$. If only the permutation matrix, \hat{f} , is known *a priori*, the parameters \hat{U} and $\hat{\mathbf{t}}$ can be computed using Horn’s algorithm³³ with complexity $O(m)$. Horn’s algorithm uses quaternions to provide a closed-form solution for aligning two point sets such that RMSD is minimized. If all of \hat{f} , \hat{U} , and $\hat{\mathbf{t}}$ are unknown, more sophisticated algorithms are required for minimizing RMSD between clusters of atoms. A good review of different techniques is provided in Ref.²⁷. For example, in Ref.²³, a two-stage method, which includes a Monte-Carlo perturbation, has been proposed for finding the global-minimum in RMSD. Another recent technique uses molecular dynamics and simulated annealing^{34,35} to align clusters, and has been used to identify first neighbor (short-) ³⁴ and first- through third-neighbor (medium-) range order³⁵ in metallic glasses. In Ref.²⁷, two efficient algorithms, GO-PERMDIST and FASTOVERLAP, were introduced. However, these techniques currently are limited to equal number of atoms in the model and the target. And, more importantly, the optimal translation $\hat{\mathbf{t}}$ that produces the best match is assumed to be known *a priori*. While this is a reasonable approximation when $n = m$, determining the translational component is non-trivial when the two structures to be compared have different number of atoms.

A. An Illustration of the Two-Dimensional Point-Pattern Matching Algorithm

Here we present a new Point-Pattern Matching (PPM) algorithm based on graph theory arguments developed by McAuley and Caetano³⁶. This technique is general enough to be applied for systems with different number of atoms. While Ref.³⁶ contains complete details of the rigid-graph PPM algorithm, in this section, we provide an illustration of the steps in the algorithm for point-sets in two-dimensions.

Figure 1(a, b) show the model and the target, respectively. The objective is to identify the set of points in the target that best match the model point-set. In Ref.³⁶, a graph representation of a point-set is used to identify the optimal permutation mapping \hat{f} . The sets

of points in the model \mathbf{M} and target \mathbf{T} can be expressed as graphs by using the information contained in the atom positions (nodes) and bonds (edges). Usually, a graph is defined by the set of nodes and edges (V, E) . We will, however, consider a graph \mathcal{G} to be a set of pairs of nodes, and say $(i, j) \in \mathcal{G}$ if an edge connecting nodes i and j is present in graph \mathcal{G} (using the notation developed in Ref.³⁶). The complete graphs, which contain all the possible edges in the point-set, representing the model and the target will be denoted by \mathcal{M} and \mathcal{T} , respectively.

Instead of using RMSD defined in Eq. 1, McAuley and Caetano introduced a metric that depends only on edge lengths and hence is invariant to rotations and translations. This metric, for a given permutation function f , is defined on the graphs and is provided in Eq. 2. The objective of the PPM technique is to determine the function \hat{f} that minimizes the metric $\mathcal{D}(f)$ as defined in Eq. 3.

$$\mathcal{D}(f) = \sum_{(i,j) \in \mathcal{M}} |d(\mathbf{r}_i^M, \mathbf{r}_j^M) - d(\mathbf{r}_{f(i)}^T, \mathbf{r}_{f(j)}^T)| \quad (2)$$

$$\hat{f} = \arg \min_{f: \mathcal{M} \rightarrow \mathcal{T}} \mathcal{D}(f) \quad (3)$$

The mapping \hat{f} produces a matching between the points in the model and the target, such that the sum of the differences in all the edge lengths is minimized. This definition allows for computing optimal mappings even in the presence of noise. The algorithms to determine \hat{f} fall under the class of quadratic assignment problems, which are in general NP-hard³⁷. In Ref³⁸, McAuley *et al.* introduced the concept of a rigid-graph to solve the matching problem in an efficient manner. A rigid-graph is a subset of the original graph such that the only transformations that can be applied to the node coordinates while preserving the distances in the rigid-graph are isometries (rigid-body translations and rotations). If the rigid-graph of the model \mathcal{M} is denoted by \mathcal{R} , then the new objective function can be written as:

$$\hat{f} = \arg \min_{f: \mathcal{R} \rightarrow \mathcal{T}} \mathcal{D}(f) \quad \text{where} \quad \mathcal{D}(f) = \sum_{(i,j) \in \mathcal{R}} |d(\mathbf{r}_i^M, \mathbf{r}_j^M) - d(\mathbf{r}_{f(i)}^T, \mathbf{r}_{f(j)}^T)| \quad (4)$$

where \mathcal{M} is replaced by the rigid-model-graph \mathcal{R} . The difference between \mathcal{M} and \mathcal{R} is the number of edges considered during the minimization. For example, a complete graph, where all the possible edges in the model point-set are considered to be a part of the graph, is

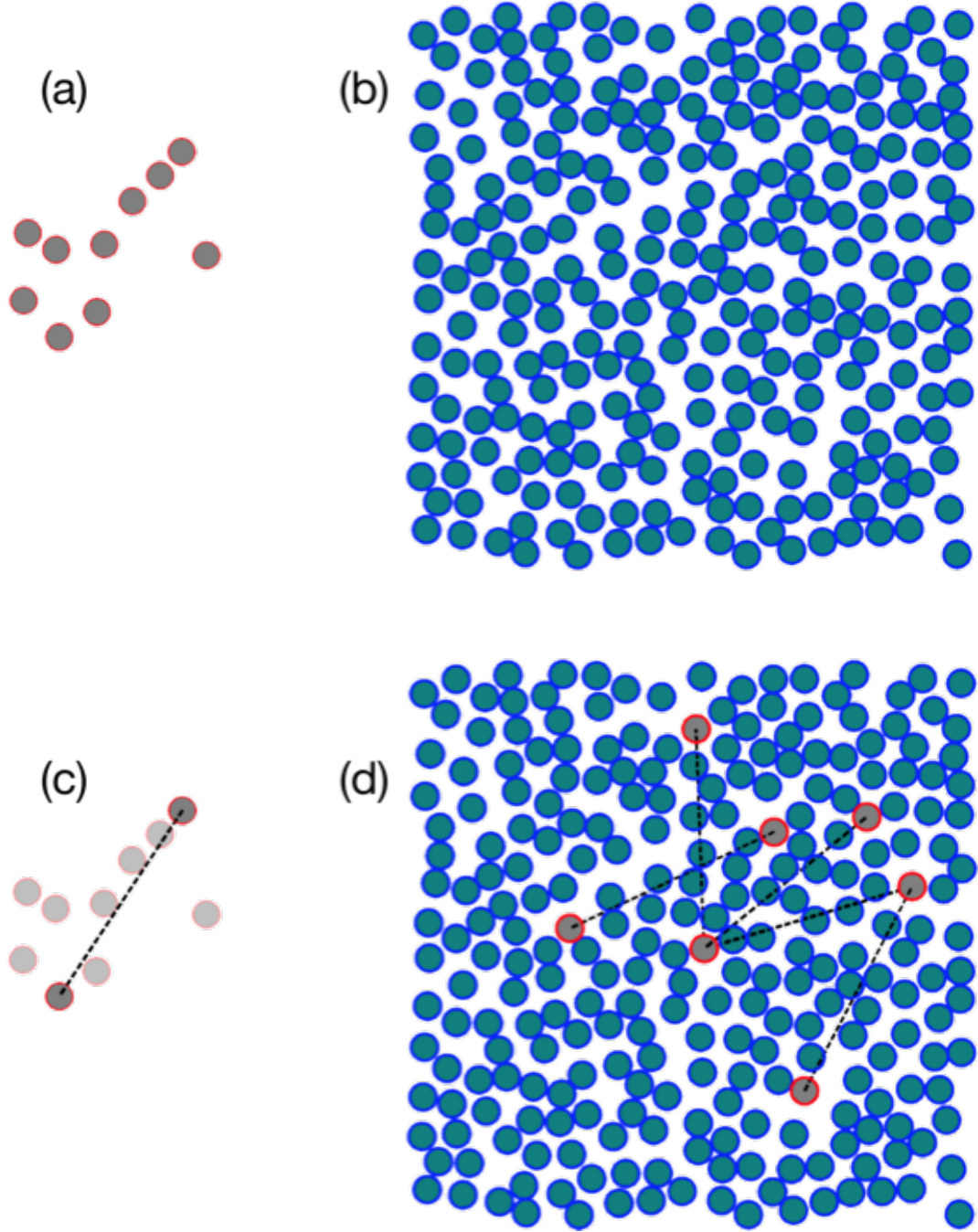


FIG. 1. The model and target point-sets are shown in (a) and (b), respectively. The points are represented using discs to illustrate atoms in this example. In (c), the two root nodes in the model are highlighted. In (d), a few example pairs of points in the target that match the root nodes are illustrated.

shown in Figure 2 (a). In this complete graph, there are $m(m-1)/2 = O(m^2)$ edges. As defined in Ref.³⁶, the rigid graph for a two-dimensional (2D) point-set is constructed by first choosing two nodes that are connected by an edge. These two points are usually referred

to as the *root nodes*. All the other points in the model are then connected to the two root nodes as shown in Figure 2 (b). Therefore, the rigid graph of the model contains the edges between the root nodes and, instead of all the edges in the model point-set, only those edges that connect the rest of the points to the root nodes. The total number of edges in this rigid graph is $2m - 3 = O(m)$. The global rigidity theorem³⁹ implies that preserving the lengths of the edges in \mathcal{R} preserves the lengths in the complete graph of the model point-set. The required number of root nodes depends on the dimensionality of the point-set. In 2D, two root nodes are required and, in 3D, we need three root nodes to construct the rigid graph.

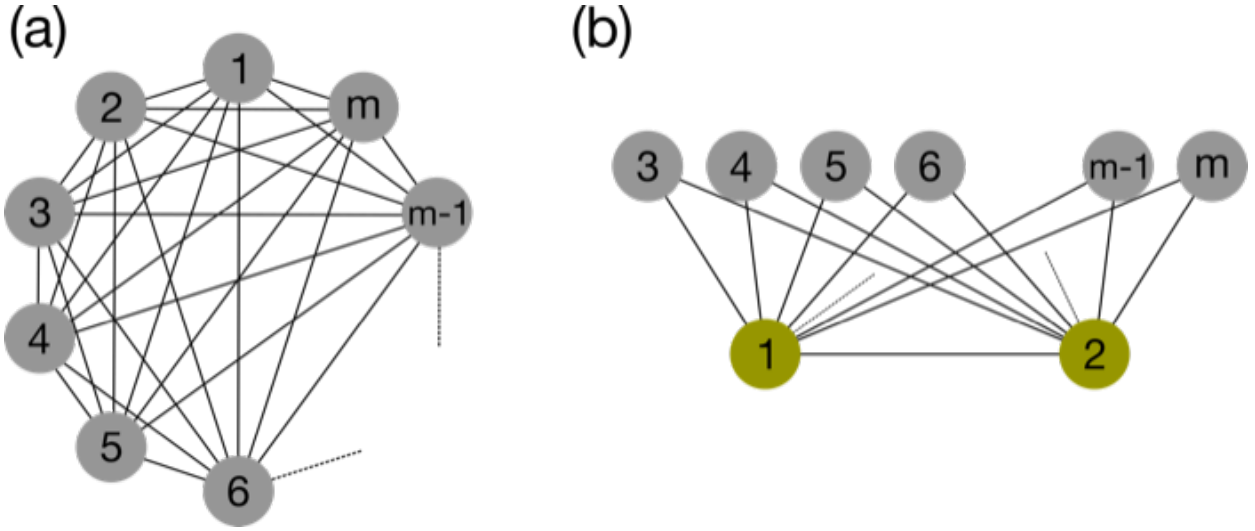


FIG. 2. (a) A complete graph with all possible edges connecting the m points in the model is shown. In (b), the rigid-graph of the model is shown. The rigid graph in two dimensions consists of the edge between the two root nodes (highlighted) and all the edges between the rest of points and the root nodes.

1. The input for the PPM algorithm contains the two point-sets and the root nodes in the model. The choice of the root nodes does not influence the accuracy of the algorithm but if the root nodes are chosen judiciously, the run-time for obtaining the solution can be reduced. We are interested in minimizing the sum of differences in the edge lengths in the rigid graph of the model and the mapped point-set in the target (Eq. 4). We assume that these differences scale as the actual edge length. Therefore, picking the nodes that contain the largest edge as the root nodes can improve the efficiency of the algorithm. With this assumption, we choose the two nodes that are farthest apart as root nodes in 2D. The root nodes for the model are shown in Figure 1(c). In 3D, we choose three nodes where the sum of the edge lengths of the triangle is maximized.

2. Once the root nodes are fixed, we find all possible matches in the target for the root nodes. In 2D, the computational cost is $O(n^2)$. This is equivalent to enumerating all possible pairs of points in the target. In 3D the cost is $O(n^3)$ as three root nodes are required. Some of the matches for the root nodes in the target are shown in Figure 1(d). Consider the best match for the root nodes, as shown in Figure 3(a, b). A local coordinate system is defined with the root nodes in the model (Figure 3(a)) and the matched-root-nodes in the target (Figure 3(b)).
3. For each remaining point in the model, the vector in the local coordinate system is computed (as shown for two points in the model in Figure 3(c)). An equivalent vector in the target is then defined using the local coordinate system in the target (Figure 3(d)). A nearest-neighbor algorithm is then used to determine the point n_p that is closest to the equivalent vector in the target. For the two vectors in the model, equivalent vectors and the nearest points are shown in the target in Figure 3(d). The algorithmic complexity to determine the nearest point is $O(\log n)$ (using a KD-tree data-structure).
4. Finally, the steps described above are repeated for all the remaining points in the model (Figure 4(a)). The points in the target that best match the model are shown in Figure 4(b).
5. In Figure 4(c), the alignment between the model and the mapped points are shown by overlapping points. To align the two point patterns, the rotation U and rigid body translation \mathbf{t} that minimizes the RMSD metric defined in Eq. 1 is computed using Horn's algorithm³³, which has a complexity of $O(m)$.

The complexity of the point pattern matching algorithm to compute \hat{f} is determined by combining the complexities in steps 1-3 and is given by $O(mn^d \log n)$, where $d = 2, 3, \dots$ is the dimensionality of the point-set. The PPM algorithm is made reasonably efficient by using a rigid-graph representation (so as to reduce the total number of edge-lengths to be matched), and by using the k -nearest neighbor algorithm for identifying similar points in the model and the target. The Horn's algorithm in the last step adds an additional computational cost of $O(m)$ but the dominant terms come from the PPM algorithm.

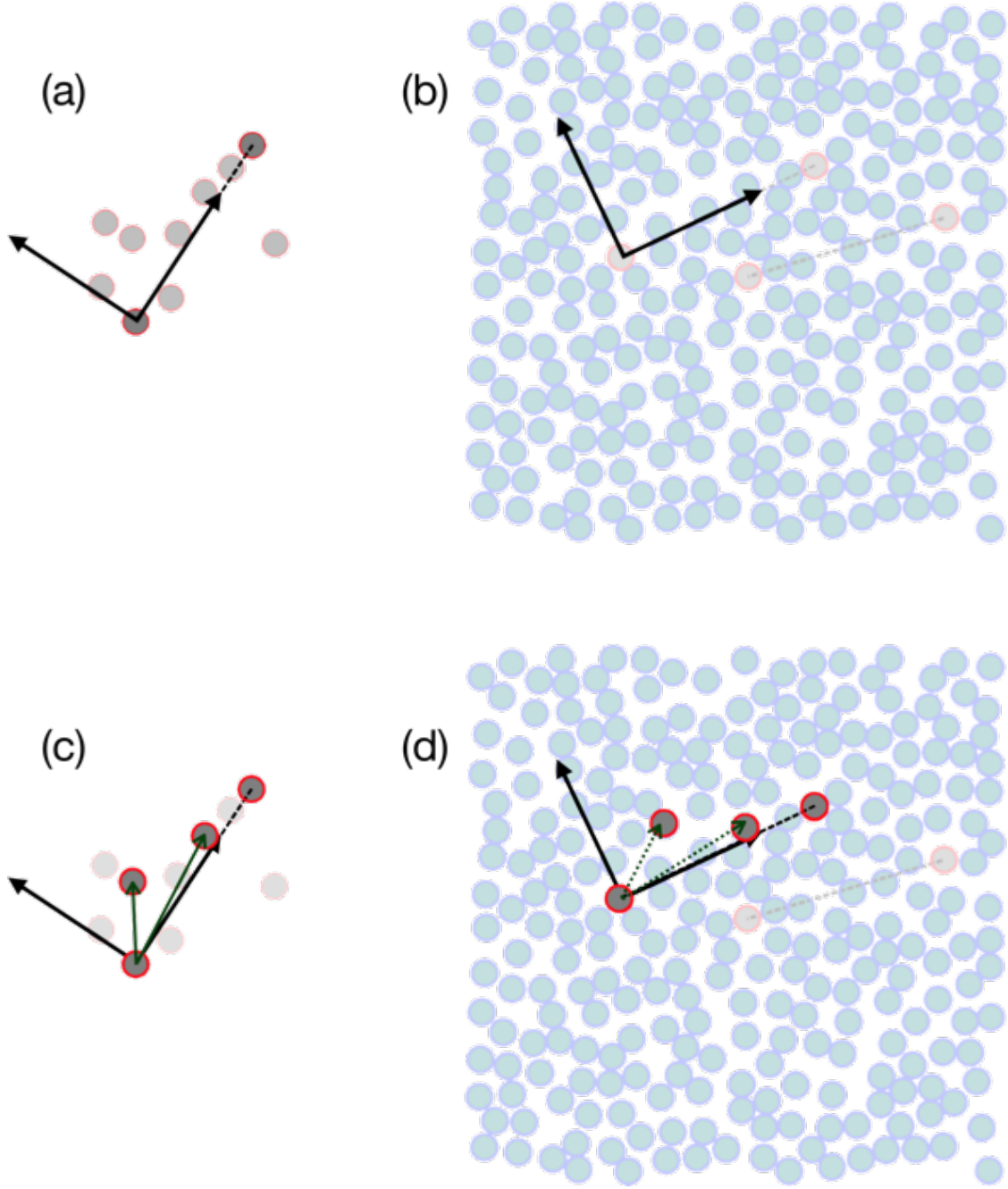


FIG. 3. The local coordinate systems, defined by the root nodes, are illustrated in the model and the target in (a) and (b), respectively. In (c) the vectors of two points (other than the root nodes) in the model are shown and in (d) the equivalent vectors are shown using dotted lines. The highlighted points in (d) are the nearest-points to the equivalent vectors in the target.

In Figure 5, we illustrate the complexity of the algorithm by comparing clusters of equal and unequal number of atoms, respectively. For the red curve, there are equal number of points in the model and target (i.e. $n = m$), and for the blue curve the number points in the model is fixed ($m = 10$) and the number of points in the target are varied. The

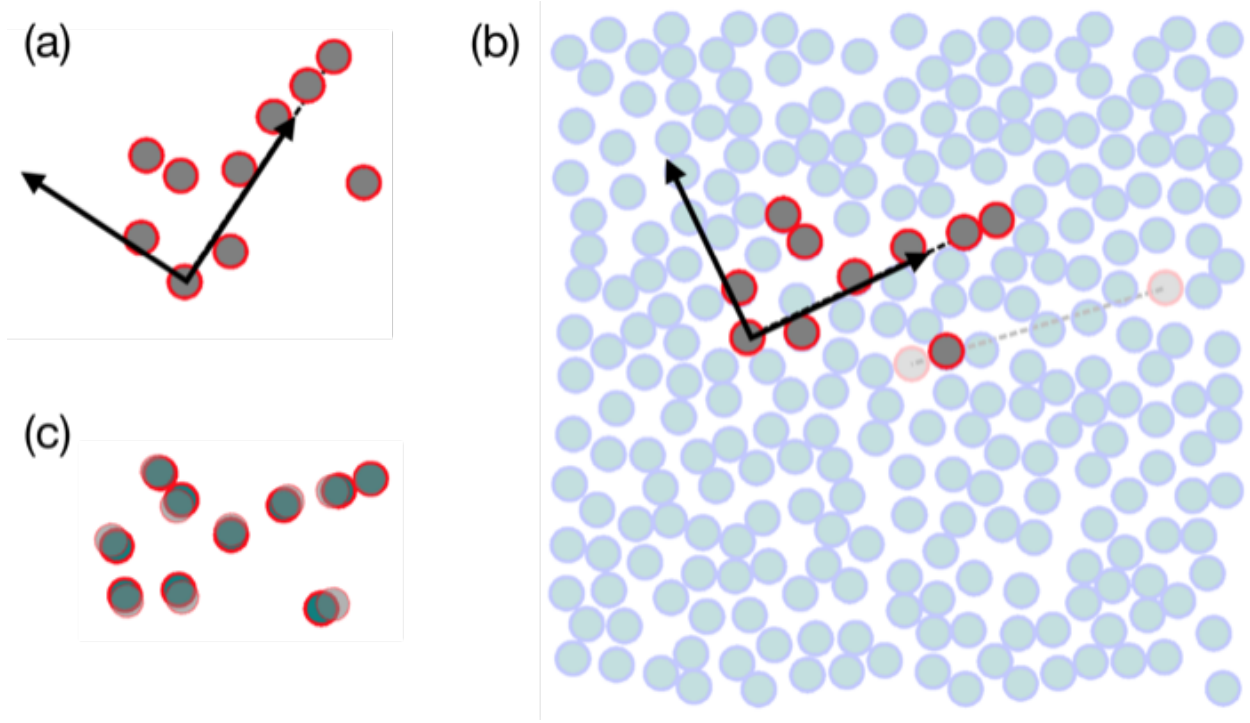


FIG. 4. The model point-set with the local coordinate system is shown in (a). The best match found in the target point-set is shown in (b). In (c), the registration between the model and the mapped-points in the target, which is obtained using Horn's algorithm, is shown.

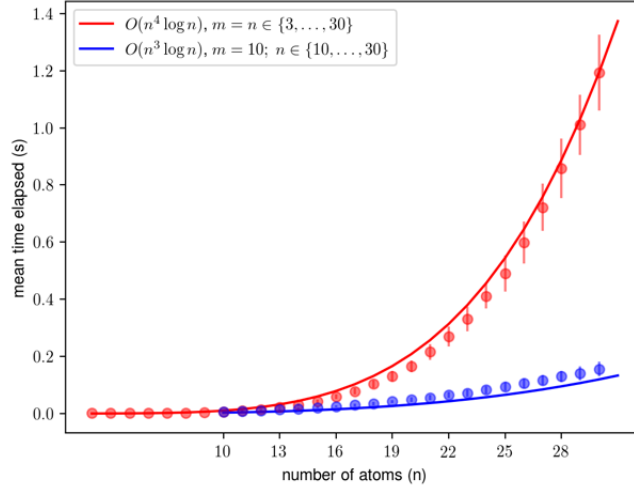


FIG. 5. Performance scaling for the PPM algorithm as a function of the number of points in the model and target sets are shown. The tests are performed for equal number of points in both the model and target, i.e. $n = m$ and are shown in the red curve. The scaling with a fixed number of points in the model set ($m = 10$) and increasing number of points in the target is shown in the blue curve. The point sets are three-dimensional and the scaling is $O(mn^3 \log(n))$.

target point-sets are created by picking random points in three-dimensions with the x , y and z coordinates in the interval $[-1, 1]$. The model set is created by picking a random subset of the target, adding a Gaussian random noise (with $\sigma = 0.1$) to the points, and randomizing the indices. The alignments are performed on a standard desktop computer (Intel Xeon quad-core processor, 1.80 GHz, 4 GB RAM) and the asymptotic scaling of $O(mn^3 \log n)$ for three-dimensional point-sets is shown in Figure 5. The PPM algorithm is coded in C++, with a Python wrapper to promote ease of use, and is shared online at <https://github.com/spatala/ppm3d>. The python wrapper has been implemented with capabilities for parallelization on a distributed computing platform, such as HTCondor⁴⁰, for applications where millions of alignments have to be performed.

B. Potential Applications

PPM is particularly useful when the number of atoms in the clusters being compared is not the same and the translation vector $\hat{\mathbf{t}}$ is not known. Several important problems in condensed matter systems, both within materials science and in other fields, fall in this category. A few examples problems are discussed here, then results for two of them are presented in detail in the next section.

Section III A discusses the problem of comparing grain boundary (GB) structures. To develop structure-property relationships for crystalline interfaces, it is necessary to investigate structural variations as function of the crystallographic parameters⁴¹. Banadaki and Patala have developed the void-clustering algorithm to create a topological representation of a GB structure using polyhedral units¹⁸. However, the polyhedral unit representation is a topological descriptor and, as is the case with any topological descriptor, small changes in the atom positions can completely alter the polyhedral units observed in the GB. Thus, it is not robust against small perturbations in the crystallographic parameters of the GB, nor is it a continuous function of those parameters. These limitations make it impossible to use void-clustering and the polyhedral representation to compare GB structures to one another in a meaningful way. The PPM algorithm removes these limitations. As described in section III A, we use the void-clustering algorithm to define the *model* polyhedral units in *singular* GBs. Then, we use PPM to find these model units in other GBs that are *vicinal* to the singular GBs. In this problem, the model structure (the polyhedral unit) and the target

(the entire vicinal GB) have very different numbers of atoms, and the optimal translations, required to identify the polyhedral units, are unknown.

Similar methodology could be used to identify near-coincident site lattices (CSLs) in special GBs.⁴² CSLs are matching lattice-sites between two crystals. These lattices can be either different phases or lattices with different orientations. The CSLs determine orientation relationships during phase transformations and are used as one of the criteria for determining the crystallography of low-energy interfaces. To date, there does not exist a general algorithm to determine all the possible CSLs (or near-CSLs) in a given material system. PPM could be used to identify the coincidence sites by enumerating sublattices and comparing them to each other. In this problem, the number of atoms in the model sublattice is significantly smaller than the number of atoms in the target phase, making this a good potential problem for PPM.

Section III B discusses the problem of characterizing local structures in metallic glasses. Metallic glasses are often represented as characteristic first-neighbor atomic clusters which pack together to make a solid⁴³. Those clusters are identified by their polyhedral shape, which for metal-metal glasses like Zr-Cu is often icosahedral^{44–46}. However, the inherent structural disorder in a glass means that only a small fraction of the polyhedra are perfectly icosahedral. Others are identified as “quasi”-icosahedral⁴³, often based on the idea that they are fundamentally an icosahedron, but with an extra atom or a missing atom due to disorder. We use PPM to test whether or not clusters with (quasi-) icosahedral topologies have icosahedral *geometry* as well. In this case, the model is a geometrically perfect icosahedron consisting of twelve atoms, and the targets are first-neighbor clusters drawn from a metallic glass model with coordination numbers varying from 9 to 16. PPM both provides the ability to match such clusters to one another and to define a quantitative and continuous similarity metric for comparison.

Beyond nearest-neighbor clusters, PPM could be used to characterize larger-scale medium-range order in metallic glasses in two ways. First, one could identify all the SRO clusters conforming to a particular geometry (*e.g.* an icosahedron), then identify if they are connected by, for example, how many atoms the connected clusters have in common. This approach is commonly used with topological structure measures. Second, PPM can be used to identify clusters with atoms outside the first-neighbor shell, provided that one can define a model geometry. Candidate model geometries could include particular connected geometries

of icosahedra (e.g. a face-sharing pair)⁴³ or larger Bergman or Mackay clusters⁴⁷. As the number of atoms in the model cluster increases, the ability to match a perfect model cluster to target clusters with varying coordination number in order to accommodate structural disorder becomes even more important.

Beyond the topics discussed here, PPM could be useful in modeling the growth of nanoclusters and mutations in biomolecules. In the area of nanoparticle synthesis and stability, different pathways along which nanoparticles grow is of interest⁴⁸. To construct these pathways using atomistic simulations, one has to compare and align clusters of different sizes. These comparisons are also necessary for calculating free energies and rates of different pathways. Mutation of biomolecules has a parallel “pathways” problem, as we often wish to track changes as a function of generation and calculate free energies and rates along the way.⁴⁹ Since the number of atoms change during the growth and mutation processes, PPM is well-suited to this task.

Finally, the PPM algorithm can also be utilized when the extent of overlap between the model and the target point-sets is incomplete. That is, when there are outliers in the model point-set that do not match with points in the target. Such outliers are referred to as *occlusions*⁵⁰ in the image-processing literature. When occlusions are allowed, the PPM algorithm finds the largest subset of the model and the target that results in the best possible matching. This capability is particularly useful when there is a limited overlap between the clusters being compared, *e.g.* when identifying binding regions between proteins.^{51,52}

III. RESULTS AND DISCUSSION

A. Local Atomic Motifs in Grain Boundaries - A Three-Dimensional Polyhedral Unit Model

GBs are planar defects in polycrystalline materials and influence a wide array of structural and functional properties⁵³. Unfortunately, GBs are also one of the least understood defect types in materials science. This is due to the vast and topologically complex, five-dimensional crystallographic degrees-of-freedom (DOF) of a GB^{54–56}. The five dimensions correspond to the so-called macroscopic degrees of freedom - three parameters define the misorientation between individual grains and the other two fix the boundary-plane orien-

tation. These parameters constitute the bicrystallographic aspects of interfaces. One of the primary objectives of grain boundary engineering has been to predict structure and properties of GBs as a function of the five crystallographic parameters.

From a geometrical perspective, the structure of certain GBs (those with low-index planes at the interface) has traditionally been represented using clusters of atoms that form quasi-two-dimensional geometrical motifs. This model, referred to as the structural unit model (SUM), was first proposed by Bishop and Chalmers⁵⁷ and has been extended to a variety of tilt GBs by Sutton and Vitek^{58,59}. More recently, Han et al. developed a framework utilizing the metastable-SUM to predict GB structures and energies for [100] and [111] symmetric-tilt GBs⁴¹. They emphasized that the metastable-SUM framework can be used to describe structural variations in the complete five-dimensional crystallographic phase-space of GBs. One of the key steps in this framework relies on *identifying pre-determined geometrical motifs in a variety of minimum-energy and metastable GB structures*. Identifying three-dimensional geometrical motifs in complex, disordered GBs is difficult, but the PPM algorithm is uniquely suited to address this issue.

Rather than focusing on the physical aspects of GB properties, here we show a simple example to illustrate how the PPM algorithm can be used to describe structural variations in GBs as a function of crystallographic parameters such as misorientation angle. We will use the polyhedral units⁶⁰ to compare GB structures, instead of the somewhat arbitrarily defined structural units. We can use the void-clustering algorithm¹⁸, which is based on the clustering of voids present in the GB structure, to automate the process of representing a GB structure as a combination of polyhedral units. We then want to use this representation to compare the atomistic structures of different GBs with similar crystallography. As mentioned previously, the void-clustering algorithm by itself cannot reach this goal. Instead, we adopt a two-step procedure in which void-clustering is first used to identify the model polyhedral units in the *singular* GBs. Singular GBs correspond to cusps in the energy landscape⁶¹, so their structure is less sensitive to perturbations. Then, we use the PPM technique to identify the polyhedral units found in the singular boundaries (the model point-sets) in the vicinal GB structures (the target point-sets). Quantifying the density and the spatial arrangement of the model polyhedral units will provide a direct link between the properties of the singular and the vicinal GBs^{41,62}. To illustrate this two-step process, we analyze the set of [100] symmetric tilt GBs in aluminum with the misorientation angle ranging from

36.87° to 53.13°. Figure 6 shows the energies of the [100] symmetric tilt GBs as a function of the tilt angle.

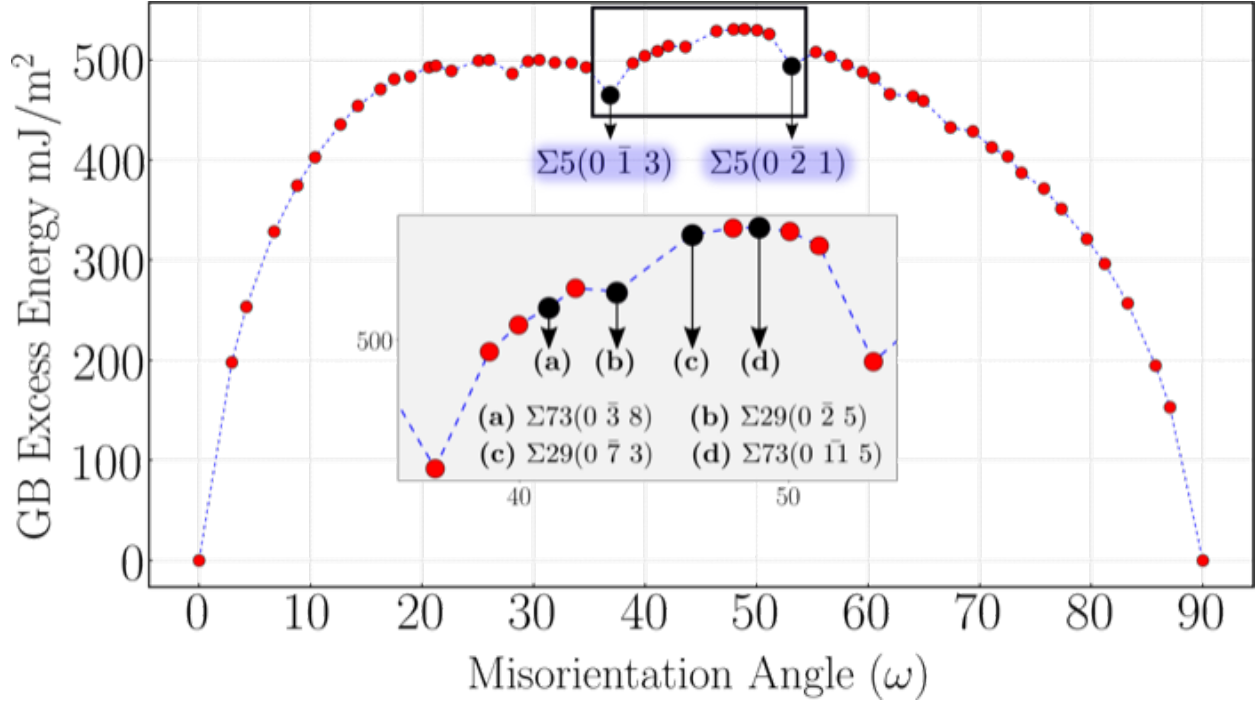


FIG. 6. The energy of grain boundaries in aluminum as a function of misorientation angle. The energies of the [100] symmetric tilt GBs and the other GBs analyzed in detail ((a) - (d)) are marked with arrows and labeled with their crystallographic elements.

The first step is to identify the polyhedral units in the singular GBs. In Figure 6, the two singular $\Sigma 5$ GBs, corresponding to cusps in the energy landscape, are highlighted. Banadaki and Patala showed that 11-atom polyhedra, which can be viewed as distorted octadecahedra⁶³, are observed in these two $\Sigma 5$ GBs.¹⁸ Figure 7 shows their atomistic structures and polyhedral unit representations.

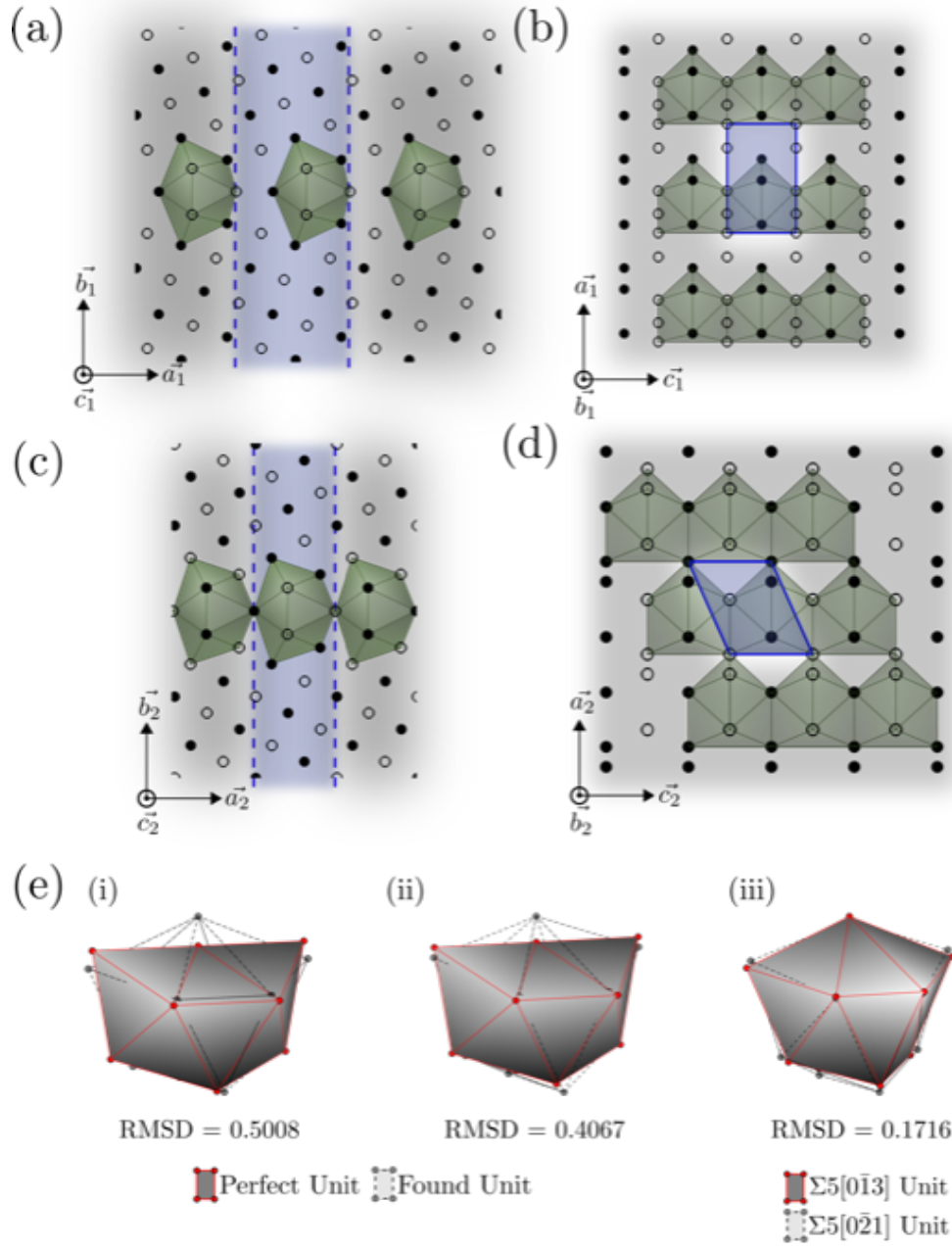


FIG. 7. The atomistic structure of $\Sigma 5(0\bar{1}3)$ and $\Sigma 5(0\bar{2}1)$ with the 11-atom polyhedral units highlighted. The views in (a, c) are along the tilt axis, $[100]$, and (b, d) are along the boundary-plane normal. In (e) the RMSD of the observed polyhedral units compared to the perfect octadecahedra and compared to each other is reported. The “Found Unit” in the legend of (e, i) and (e, ii) refers to the unit observed in the $\Sigma 5(0\bar{2}1)$ and $\Sigma 5(0\bar{1}3)$ GBs, respectively. The axes in the (a, b) are such that, $\vec{a}_1 = [031]$, $\vec{b}_1 = [0\bar{1}3]$ and $\vec{c}_1 = [100]$. The axes in (c, d) are, $\vec{a}_2 = [012]$, $\vec{b}_2 = [0\bar{2}1]$ and $\vec{c}_2 = [100]$.

The second step is to use the PPM algorithm to compare the structures of the two singular $\Sigma 5$ GBs with the vicinal GBs ($\Sigma 29$ and $\Sigma 73$ GBs, also highlighted in Figure 6). That is, we want to identify the octadecahedral units (the model point-sets, containing 11 atoms) in the vicinal GB structures (the target point-sets, containing many atoms). For example, in the $\Sigma 73(0\bar{1}15)$ GB, there are about 265 atoms in the GB structure. The optimal translation vector $\hat{\mathbf{t}}$ is also unknown.

The octadecahedral units identified using the PPM algorithm in the $\Sigma 29(0\bar{2}5)$ and $\Sigma 29(0\bar{7}3)$ GBs are shown in Figure 8. The octadecahedra found in the structures of $\Sigma 73(0\bar{3}8)$ and $\Sigma 73(0\bar{1}15)$ GBs are shown in Figures S1 and S2, respectively, in the Supplementary Information. These results show that the structures of the $\Sigma 73$ and $\Sigma 29$ vicinal GBs can be expressed as a combination of the octadecahedral units observed in the singular $\Sigma 5$ GBs. The variations in the tilt angle are accommodated by changing the spatial arrangement of the octadecahedral units and by adding “gaps” between the units. These gaps correspond to the **B** or **I** structural units from the perspective of the SUM⁶⁴ or the dual-tetrahedra and octahedra from the perspective of the polyhedral unit model¹⁸.

The physical significance of comparing GB structures like this has been extensively discussed in the literature.^{41,58,59,62,65} For example, Han *et al.* showed that interfacial energies can be predicted for the [100] and [111] symmetric tilt GBs in BCC tungsten over the entire misorientation range based on atomistic simulations of only four delimiting, singular GBs,⁴¹ and Balluffi has proposed a simple model for predicting properties, such as diffusivity, of symmetric tilt GBs using the structural unit model and the properties of singular interfaces.⁶² The ability to express the structure of vicinal GBs as combinations of polyhedral units that are characteristic of particular low-energy, singular GBs, therefore, allows us a straightforward way to understand and predict their properties. The combination of void-clustering and PPM described here represents a powerful tool for developing quantitative structure-property relationships for complex GBs, *i.e.* interfaces with mixed crystallographic character in the complete five-dimensional phase-space.

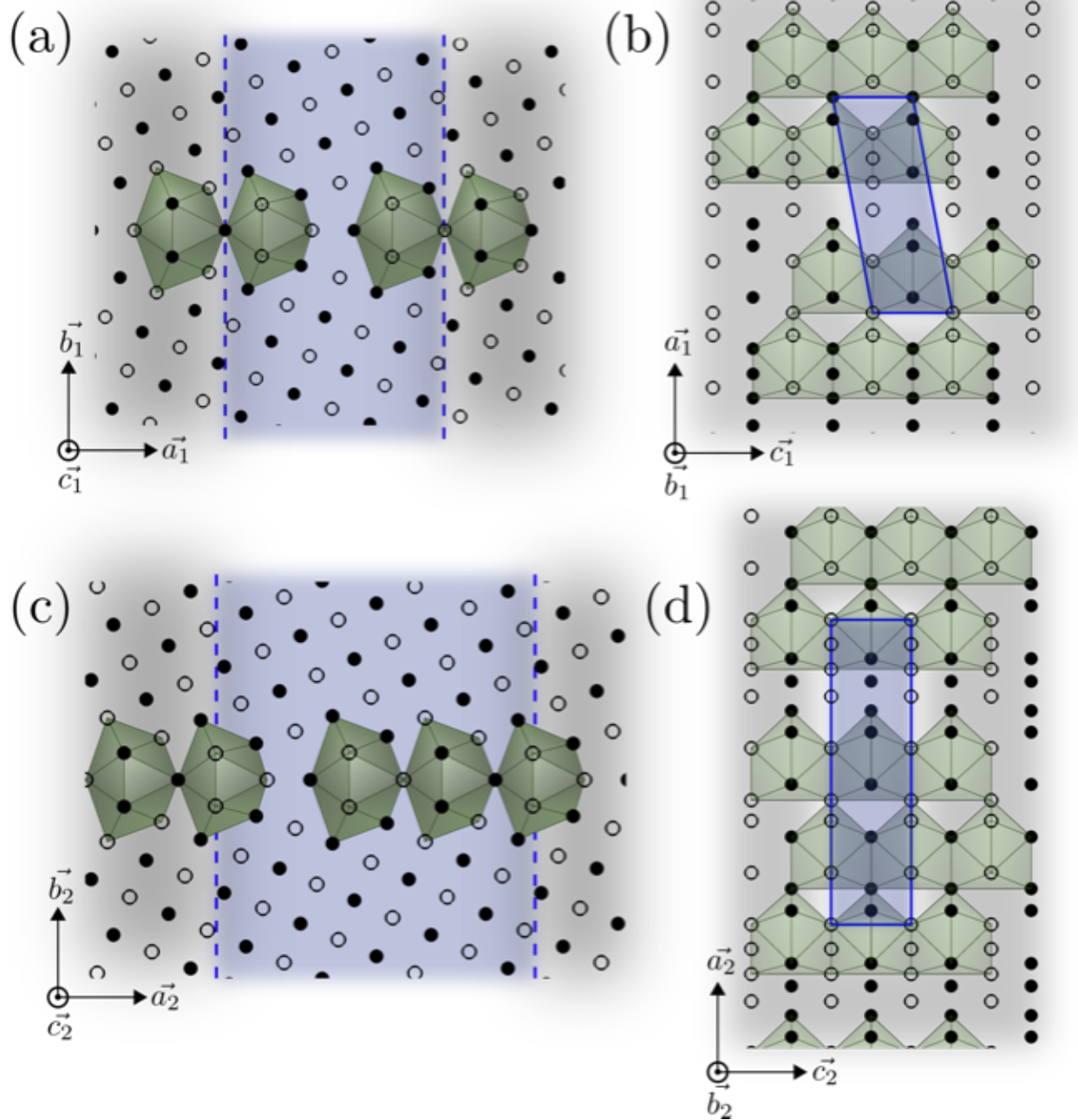


FIG. 8. The atomistic structure of $\Sigma 29(0 \bar{2} 5)$ and $\Sigma 29(0 \bar{7} 3)$, with the 11-atom polyhedral units highlighted, in (a, b) and (c, d). The views in (a, c) are along the tilt axis and (b, d) are along the boundary-plane normal. The axes in the (a, b) are such that, $\vec{a}_1 = [0 5 2]$, $\vec{b}_1 = [0 \bar{2} 5]$ and $\vec{c}_1 = [100]$. The axes in (c, d) are, $\vec{a}_2 = [0 3 7]$, $\vec{b}_2 = [0 \bar{7} 3]$ and $\vec{c}_2 = [100]$.

B. Local Structure in Metallic Glasses - The Quasi-Icosahedral Clusters

Metallic glasses (MGs) are disordered materials, and their lack of long-range translational symmetry necessitates a rigorous understanding of their short- and medium-range order (SRO and MRO) structure. SRO in MGs is comprised of an atom and its nearest neighbors, which we have been referring to as a cluster. SRO balances efficient packing on one hand and chemical ordering on the other⁶⁶. Efficient packing of clusters without long-range translational symmetry requires the structure of the material to be disrupted, and therefore identifying the structural units that cause this disruption and lack of connectivity at the short-range length scale is of considerable interest. For example, in Zr-Cu based MGs icosahedra with 5-fold symmetry (which cannot tile 3D space) are the dominant SRO structural motifs^{43–46}. In addition, the distribution of clusters such as icosahedra can have a profound influence on the mechanical properties of bulk metallic glasses¹. For further information, a review on MG structure can be found in Ref⁴⁵.

Characterization of clusters in MGs is done most often using Voronoi indices, the p -vector of the number of three-, four-, five-, and six-sided faces. For example, in Zr-Cu based glasses, the atoms with icosahedral SRO are identified as those with Voronoi indices $\langle 0\ 0\ 12\ 0 \rangle$. However, the clusters will not have a perfect icosahedral geometry due to the inherent disorder in the glass. In addition, previous studies classified some Voronoi indices with a high number of pentagonal faces and geometry intuitively related to an icosahedron as *quasi*-icosahedral⁴³, even if they contain 11 or 13 atoms. However, while the quasi-icosahedral Voronoi polyhedra resemble an icosahedron, a quantitative basis for this consideration is lacking due to the topological nature of the Voronoi method.

Here, we employ the PPM algorithm to analyze the atomic structure of a $\text{Zr}_{50}\text{Cu}_{45}\text{Al}_5$ model glass. Similar glasses have been studied using other alignment methods. For example, Fang *et. al*⁴⁷ studied a Cu-Zr MG using their atomic cluster alignment method⁶⁷ and identified SRO and MRO structures in the glass. The cluster alignment method uses a collective alignment scheme to align a set of hundreds to thousands of clusters simultaneously and collectively. The collective alignment is excellent at identifying the overarching structure of a set of clusters, but is not adept at quantifying the similarity or difference of pairs of clusters as the PPM algorithm does. Here we use PPM to address the following two questions about the $\text{Zr}_{50}\text{Cu}_{45}\text{Al}_5$ model glass:

1. How distorted are the clusters with Voronoi topology $\langle 0\ 0\ 12\ 0 \rangle$, when compared to a geometrically perfect icosahedron? and
2. How similar are the clusters whose Voronoi polyhedra have a high number of 5-sided faces (some of which are considered quasi-icosahedral) to a perfect icosahedron?

The $\text{Zr}_{50}\text{Cu}_{45}\text{Al}_5$ model used in this work was obtained by quenching a liquid with that composition with 9,826 atoms from 2000 K to 600 K at 5×10^{10} K/s using molecular dynamics in LAMMPS⁶⁸ using the Sheng embedded atom model potential⁴⁶, updated in 2012. After quenching, the glass was equilibrated for 500 ps and the inherent structure was calculated by performing a conjugate gradient minimization of the potential energy. We extracted every cluster from this model. The Voronoi index distribution of these clusters is identical to those of other models produced by the same potential⁴⁶. The coordination number distribution of the clusters is shown in Figure 9(a). Coordination number twelve is the most common, consistent with icosahedral SRO. For each cluster, the bond lengths from the center atom to its nearest neighbors were normalized so their average value was 1.0, then each cluster was compared to a perfect icosahedron using PPM. Normalizing bonds lengths before matching with PPM is not required by the algorithm, and we have tested the method both with and without normalization. In this case, our goal is to test whether icosahedral topology is a good predictor of icosahedral geometry, so we elected to normalize the bond lengths before PPM, which provides a better match to topological measures of icosahedra. For example, normalizing the bond lengths makes alignment against a perfect icosahedron less sensitive to the composition of the clusters. Without normalization, PPM would report a better match to an icosahedron for a Zr-rich, Al-centered cluster with longer but uniform nearest-neighbor distances than for a cluster closer to the mean composition of the glass. In cases where the bond-lengths / relative atomic radii are important, differences in the radii can be easily recover, as they the normalization factors are recorded by the code. Horns algorithm also calculates the optimal scaling factor when comparing clusters of different sizes (once the mapping between the indices is obtained using the PPM algorithm).

After alignment, three metrics in addition to the objective function, RMSD, were calculated for each cluster comparing it to the perfect icosahedron: L^1 , L^{inf} , and a measure of angular variance, V_A . In this section we refer to RMSD as L^2 to highlight the connection

between RMSD, L^1 , and L^{inf} . These metrics are defined by:

$$\begin{aligned}
L^1(\mathbf{M}, \mathbf{T}) &= \frac{1}{m} \sum_{i=1}^m |\hat{\mathbf{r}}_i^M - \mathbf{r}_{f(i)}^T| \\
L^{inf}(\mathbf{M}, \mathbf{T}) &= \max(\hat{\mathbf{r}}_i^M - \mathbf{r}_{f(i)}^T) \\
V_A(\mathbf{M}, \mathbf{T}, c) &= \frac{1}{N} \sum_{n=i,j}^N |\angle(\hat{\mathbf{r}}_i^M, \mathbf{0}, \hat{\mathbf{r}}_j^M) - \angle(\mathbf{r}_{f(i)}^T, \mathbf{0}, \mathbf{r}_{f(j)}^T)|
\end{aligned} \tag{5}$$

where m is the number of points in the model and target, $\hat{\mathbf{r}}_i^M = U\mathbf{r}_i^M + \mathbf{t}$ is the position of point i in the model point-set after rotation and translation, and the \max in L^{inf} runs over the indices $i \in [1, m]$. N is the number of neighbors (bonds) in the model where two points are neighbors if they are within a distance c of one another, $\angle(\cdot, \mathbf{0}, \cdot)$ is the angle between a pair of points going through the center of the point-set, and the summation over $n = i, j$ in V_A includes all pairs of neighbors in the point-set. In this work we define neighbors using the cutoff $c = 3.6 \text{ \AA}$, which is the first minimum in the total radial distribution function.

These four metrics were chosen to quantify various aspects of the differences in atomic structure as well as to illustrate the ability to calculate various structural similarity metrics after alignment by PPM. L^1 puts less emphasis on outliers (poorly matching atoms in the model and the target) than L^2 , while L^{inf} only considers the worst outlier. V_A provides a measure of angular variation to complement the bond length measures of the L^p metrics. The geometric mean of these four metrics, $\sqrt[4]{L^2 \cdot L^1 \cdot L^{inf} \cdot V_A}$, was used as the final metric of comparison to the perfect icosahedron and is henceforth called the geometric mean error (GME). The GME of all the metrics was found to better separate different structures than any single metric. The geometric mean is appropriate for calculating averages of numbers with different numerical ranges and retains information about the relative change of those numbers when comparing different values.

We first consider all 2,285 clusters with coordination number 12 after alignment to a target of a perfect icosahedron. Figure 9(b) (blue) shows the distribution of the GMEs calculated after these alignments. The distribution is bimodal, and the low-GME peak is composed of geometrically icosahedral clusters. GME histograms for clusters with Voronoi indices $\langle 0 \ 0 \ 12 \ 0 \rangle$, $\langle 0 \ 2 \ 8 \ 2 \rangle$, or $\langle 0 \ 3 \ 6 \ 3 \rangle$ (orange, green, and red, respectively) illustrate the

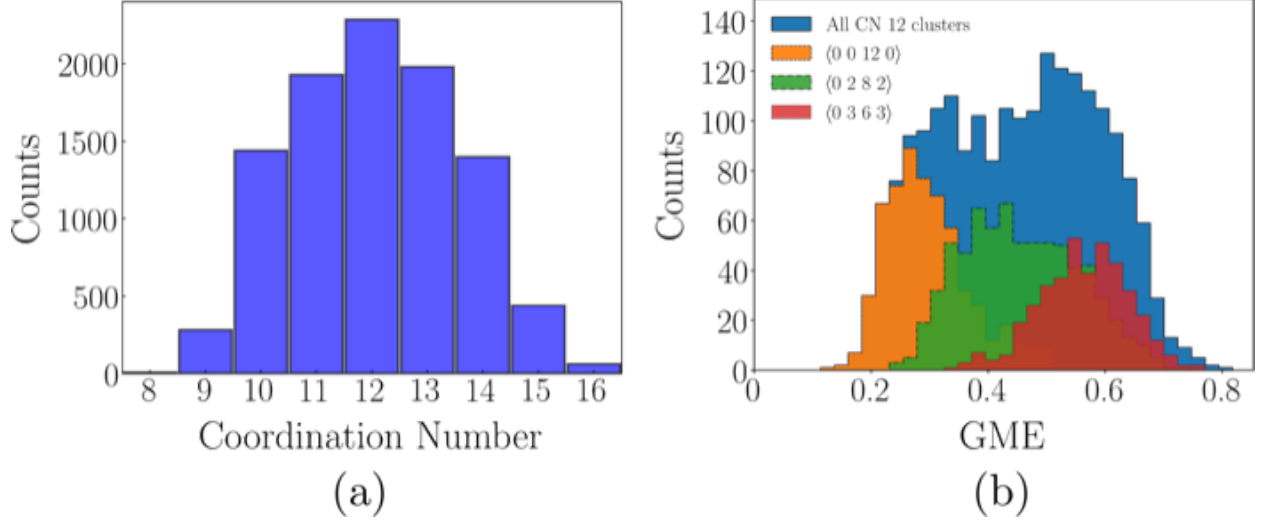


FIG. 9. (a) The coordination number distribution for the $\text{Zr}_{50}\text{Cu}_{45}\text{Al}_5$ metallic glass model studied in this section. (b) The bimodal distribution (blue) of GMEs for all 2,285 clusters with coordination number 12 in the MG model. The colors show analogous histograms for the sets of clusters with three different Voronoi indices, all of which have coordination number 12.

range of GME values associated with clusters with these different topologies.

Next we consider all of the clusters in the model, regardless of coordination number, but still aligned against the icosahedron. Figure 10 shows the mean and standard deviations of the GME for clusters with the most common topologies, categorized by their Voronoi indices. The clusters with Voronoi indices $\langle 0\ 0\ 12\ 0 \rangle$ are most geometrically similar to the perfect icosahedron, consistent with the MG literature, as shown by their notably low mean GME. The Voronoi indices that are most often considered quasi-icosahedral include $\langle 0\ 2\ 8\ 2 \rangle$, $\langle 0\ 2\ 8\ 1 \rangle$, and $\langle 0\ 1\ 10\ 2 \rangle$ ^{45,69–72}, and while many of the clusters with these topologies exhibit a low GME, they display a wide range of distortions. In addition, the mean GME of clusters with Voronoi index $\langle 0\ 3\ 6\ 3 \rangle$ is 0.57. This value is significantly larger than the dip between the two peaks in the total histogram in Figure 9(b) at 0.42, so these clusters should not be classified as quasi-icosahedral based on their geometry. Clusters with VI $\langle 0\ 0\ 12\ 0 \rangle$ or $\langle 0\ 2\ 8\ 2 \rangle$ and GME greater than 0.42 tend to be Zr-centered (83% and 62%, respectively). This indicates that Zr-centered clusters with icosahedral topology tend to be more distorted than Cu- or Al- centered clusters with icosahedral topology, consistent with previous findings⁴⁶. The average composition of the nearest-neighbor shells of these same clusters is similar to the overall composition of the model, so there are no compositional abnormalities in the shells of these clusters.

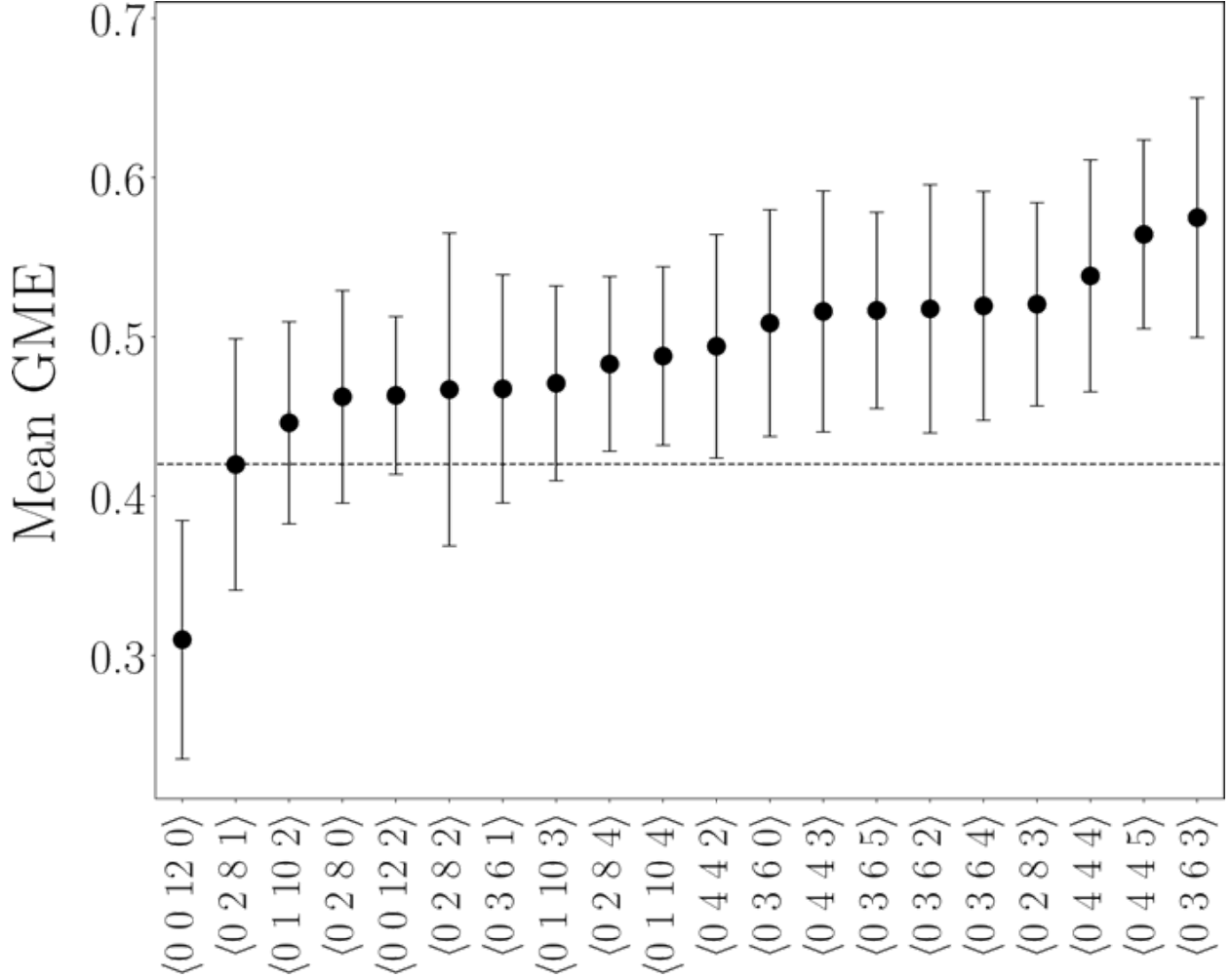


FIG. 10. The mean of the GME for clusters with specific Voronoi indices with a high number of pentagonal faces. The clusters with Voronoi index $\langle 0\ 0\ 12\ 0 \rangle$ are well below the cutoff of 0.42, while clusters with Voronoi index $\langle 0\ 3\ 6\ 3 \rangle$ are well above the cutoff and are therefore do not have icosahedral geometry despite their high number of pentagonal faces and coordination number of 12. The error bars show one standard deviation of the GME values. The horizontal dotted line designates the GME cutoff of 0.42.

The distribution of GME for $\langle 0\ 2\ 8\ 2 \rangle$ topology clusters (green in Figure 9(b)) straddles this 0.42 dividing line between icosahedral and non-icosahedral geometries, despite being widely considered quasi-icosahedral in the MG literature^{45,69–72}. Figure 11 illustrates the geometrical disparity between two $\langle 0\ 2\ 8\ 2 \rangle$ clusters. The $\langle 0\ 2\ 8\ 2 \rangle$ cluster in Figure 11(b) has a low GME of 0.25 and has similar structure to both the perfect icosahedron and the Figure 11(a) cluster with $\langle 0\ 0\ 12\ 0 \rangle$ topology and GME 0.13 (Figure 11(a)). However, the $\langle 0\ 2\ 8\ 2 \rangle$ cluster in Figure 11(c) has a large GME of 0.70 and is dissimilar in structure to both previous clusters.

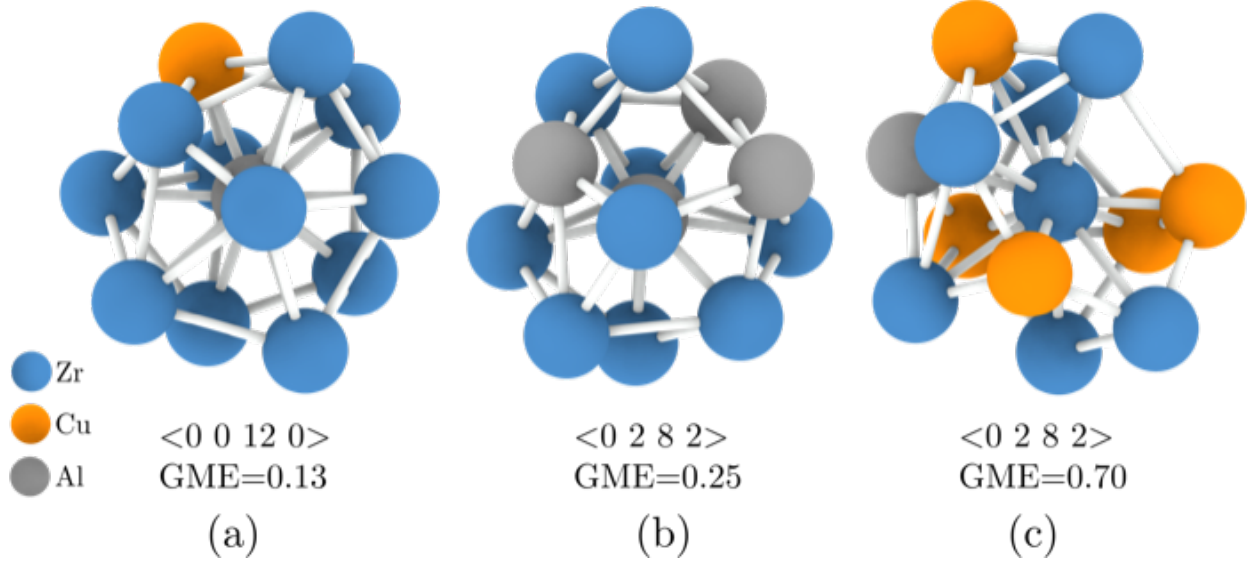


FIG. 11. Three clusters illustrate the topological insufficiency of Voronoi indices to differentiate the geometry of the structures, while the GME provides sufficient descriptive power. A $\langle 0\ 0\ 12\ 0 \rangle$ cluster (a) with low GME has similar structure to a $\langle 0\ 2\ 8\ 2 \rangle$ cluster (b) with low GME, but different structure than another $\langle 0\ 2\ 8\ 2 \rangle$ cluster (c) with high GME.

These results answer the two questions above. $\langle 0\ 0\ 12\ 0 \rangle$ topology is strongly associated with icosahedral geometry, as shown by the histogram in orange in Figure 9(b), almost all of which falls in the low-GME peak of the total distribution below the 0.42 cutoff. As illustrated in Figure 10, many of the $\langle 0\ 2\ 8\ 1 \rangle$ topology clusters are geometrically similar to a perfect icosahedron, as are many clusters with $\langle 0\ 1\ 10\ 2 \rangle$ and $\langle 0\ 2\ 8\ 2 \rangle$ topologies. However, some clusters with the latter Voronoi indices have a GME that falls above the geometrically-icosahedral cutoff of 0.42 and should not be classified as having icosahedral geometry; Figure 11(c) shows a specific example. $\langle 0\ 3\ 6\ 3 \rangle$ topologies, despite having a fairly large fraction of 5-sided faces and being sometimes considered quasi-icosahedral in the literature^{70,72} do not have icosahedral geometry based on their GME histogram. In general, PPM alignment and the GME score provides a quantitative measure of how icosahedral a cluster is in a way that Voronoi indices as a measure of topology do not. PPM and GME is a particularly useful discriminator for topologies reported to correspond to distorted, quasi-icosahedral structures.

The question of whether geometry or topology is more important for determining the influence of structure on the properties and processes of metallic glasses remains to be answered. Icosahedral topology is considered important because plastic deformation tends to

avoid regions in the structure with a high concentration of icosahedral topology⁷³; icosahedral topology regions in the supercooled liquid have slower local dynamics than other topologies^{74,75}; and the concentration of icosahedral topology increases significantly as the liquid cools through the glass transition^{45,74,75}. However, the energy of clusters depends more on their geometry (bond lengths, bond angles, coordination numbers) than on their topology, so we speculate that the explanatory power of topology arises because it is a proxy for geometry that is robust against disorder and easy to compute. PPM provides a robust, computable method of assessing geometry; future work will test its explanatory power for properties and processes in metallic glass systems.

IV. CONCLUSIONS

We have presented a point-pattern matching algorithm for local structural analysis in atomistic simulations. The PPM algorithm relies on matching the edges in the model point-set with those in the target. The complexity of the algorithm for matching point sets in three-dimensions is $O(mn^3 \log n)$, where m and n are the number of points in the model and the target, respectively. While there exist efficient algorithms for matching sets of atoms²⁷, these techniques generally assume that the optimal translation required to minimize RMSD is known *a priori*. However, when $\hat{\mathbf{t}}$ is unknown, the PPM algorithm is necessary to determine the optimal matching between the model and target point sets. PPM is capable of matching structures which do not comprise the same number of atoms.

Two examples illustrated the capabilities of the PPM algorithm. First, we analyzed the atomic structures of grain boundaries vicinal to the two singular $\Sigma 5$ GBs in aluminum. The *model* point-set is the 11-atom octadecahedral unit identified in the $\Sigma 5$ GBs using the void-clustering algorithm. The target point set is the entire atomic structure of the vicinal GBs. The PPM technique identified structures similar to the octadecahedron in the vicinal $\Sigma 29$ and $\Sigma 73$ GBs. When identifying polyhedral units in the vicinal GBs, there is no clear notion of a “center” atom that can be used as reference and, hence, the optimal translation $\hat{\mathbf{t}}$ is unknown. The number of atoms in the polyhedral unit (the model) and the GBs (the target) are also very different. Using PPM in this way enables the extension of models for predicting grain boundary properties from special structural units to more general boundaries.

Second, we illustrated the “hypothesis testing” application of PPM to discern the presence of quasi-icosahedral topologies in the atomistic structure of metallic glasses. Voronoi indices are the most common tool used to analyze short-range order in glasses. While both PPM and Voronoi indexing produce a structure descriptor, PPM provides a geometric descriptor, while Voronoi indexing produces a topological descriptor. Topological techniques are sensitive to small changes in the atomic structure, which can result in drastic, unintuitive changes in the descriptor. For the PPM geometric descriptor, small changes in the atomic structure always result in small changes in the geometric mean error descriptor. As a result, the GME of PPM-aligned clusters is a meaningful, continuous “structural distance” between two atomic structures. Both icosahedral and non-icosahedral clusters with varying coordination number were matched to a perfect icosahedron. While all of the clusters with perfect icosahedral Voronoi indices were also geometrically icosahedral, only some of the clusters with quasi-icosahedral geometry were geometrically icosahedral. Since geometry is more strongly connected to interatomic forces and energies than topology, we speculate that some of the quasi-icosahedral topology clusters with non-icosahedral geometry may have different influence the properties of the glass than their geometrically icosahedral counterparts.

More broadly, PPM has the potential to find applications in the study of a variety of materials-science and chemistry phenomena. For example, in grain boundary science and engineering, PPM could be used to identify near-coincident site lattices and their corresponding Σ -misorientations, which play a fundamental role in the analysis of interfaces both in experiments and simulations. Near-CSLs are particularly useful for identifying preferred orientation relationships between dissimilar materials⁷⁶. In metallic glasses, PPM could be used to test the hypotheses that other, non-icosahedral structures with non-crystallographic symmetry like tri-capped trigonal prisms are present in glass-forming alloys that do not exhibit icosahedra⁷⁷, and more generally to investigate the role of geometry as opposed to topology on processes like the glass transition and plastic deformation and properties like ductility. Beyond the systems studied here, PPM can be used to systematically identify the changes in atomistic structures when modeling the growth of nano-clusters or mutations in polymeric/protein molecules^{48,78–80}.

As mentioned in section II, another unique capability of the PPM algorithm is that one can allow for outliers (or occlusions) in the model point-set. This capability will be particularly useful when one is not aware of the appropriate model unit. When occlusions

are allowed, the PPM algorithm finds the largest subset of the model and the target that gives the best possible matching. When combined with an unsupervised learning algorithm, this capability can help identify atomic motifs¹⁷ that are common across large clusters of atoms.

Finally, it is of interest to improve the computational efficiency of the algorithm while being able to find the global-minima in the pattern matching. For example, a recently proposed technique, termed Go-ICP⁸¹ might provide similar results with better scaling with the size of the target. There is, however, a computational overhead as the optimization is performed in the space of rotations and translations (denoted by the group $SE(3)$). Therefore, we anticipate that for smaller cluster sizes, the PPM algorithm will more appropriate. An open-source implementation of PPM suitable for atomistic materials simulations and parallelized computation is hosted on GitHub at <https://github.com/spatala/ppm3d>.

ACKNOWLEDGEMENTS

Development of the PPM approach and application to grain boundaries by AB and SP was supported by the Air Force Office of Scientific Research Young Investigator Program funded through the Aerospace Materials for Extreme Environments (Contract # FA9550-17-1-0145). Computing resources for generating grain boundary structures was provided by the High Performance Computing Center at North Carolina State University. Implementation of the python wrapper and parallelization and application to metallic glasses by JJM and PMV was supported by NSF DMR-1332851, then by NSF DMR-1728933. The computing for parts of this research was performed using the compute resources and assistance of the UW-Madison Center for High Throughput Computing (CHTC) in the Department of Computer Sciences. The CHTC is supported by UW-Madison, the Advanced Computing Initiative, the Wisconsin Alumni Research Foundation, the Wisconsin Institutes for Discovery, and the National Science Foundation, and is an active member of the Open Science Grid, which is supported by the National Science Foundation and the U.S. Department of Energy’s Office of Science.

-
- * Corresponding Author: spatata@ncsu.edu
- ¹ J. Ding, S. Patinet, M. L. Falk, Y. Cheng, and E. Ma, Proceedings of the National Academy of Sciences **111**, 14052 (2014).
 - ² E. A. Lazar, J. Han, and D. J. Srolovitz, Proceedings of the National Academy of Sciences **112**, E5769 (2015).
 - ³ D. Barnette, Journal of Combinatorial Theory **7**, 99 (1969).
 - ⁴ E. A. Lazar, J. K. Mason, R. D. MacPherson, and D. J. Srolovitz, Physical review letters **109**, 095505 (2012).
 - ⁵ S.-H. Chang, F.-H. Cheng, W.-H. Hsu, and G.-Z. Wu, Pattern recognition **30**, 311 (1997).
 - ⁶ R. Myers, R. Wison, and E. R. Hancock, IEEE Transactions on Pattern Analysis and Machine Intelligence **22**, 628 (2000).
 - ⁷ M. Carcassoni and E. R. Hancock, Pattern Recognition **36**, 193 (2003).
 - ⁸ H. Wang and E. R. Hancock, in *Joint IAPR International Workshops on Statistical Techniques in Pattern Recognition (SPR) and Structural and Syntactic Pattern Recognition (SSPR)* (Springer, 2004) pp. 361–369.
 - ⁹ M. T. Goodrich, J. S. Mitchell, and M. W. Orletsky, IEEE Transactions on Pattern Analysis and Machine Intelligence **21**, 371 (1999).
 - ¹⁰ T. S. Caetano, J. J. McAuley, L. Cheng, Q. V. Le, and A. J. Smola, IEEE transactions on pattern analysis and machine intelligence **31**, 1048 (2009).
 - ¹¹ Y. C. Martin, M. G. Bures, E. A. Danaher, J. DeLazzer, I. Lico, and P. A. Pavlik, Journal of computer-aided molecular design **7**, 83 (1993).
 - ¹² P. W. Finn, L. E. Kavradi, J.-C. Latombe, R. Motwani, C. Shelton, S. Venkatasubramanian, and A. Yao, in *Proceedings of the thirteenth annual symposium on Computational geometry* (ACM, 1997) pp. 324–333.
 - ¹³ F. Murtagh, Publications of the Astronomical Society of the Pacific **104**, 301 (1992).
 - ¹⁴ G. Weber, L. Knipping, and H. Alt, Journal of Symbolic Computation **17**, 321 (1994).
 - ¹⁵ T. Akutsu, K. Kanaya, A. Ohyama, and A. Fujiyama, Discrete Applied Mathematics **127**, 5 (2003).

- ¹⁶ R. Nussinov and H. J. Wolfson, Proceedings of the National Academy of Sciences **88**, 10495 (1991).
- ¹⁷ J. J. Maldonis, A. Banadaki, S. Patala, and P. M. Voyles, In Preparation.
- ¹⁸ A. D. Banadaki and S. Patala, npj Computational Materials **3**, 13 (2017).
- ¹⁹ J. Salvi, C. Matabosch, D. Fofi, and J. Forest, Image and Vision computing **25**, 578 (2007).
- ²⁰ A. A. Goshtasby, *Image registration: Principles, tools and methods* (Springer Science & Business Media, 2012).
- ²¹ E. A. Coutias, C. Seok, and K. A. Dill, Journal of computational chemistry **25**, 1849 (2004).
- ²² A. P. Bartók, M. C. Payne, R. Kondor, and G. Csányi, Physical review letters **104**, 136403 (2010).
- ²³ A. Sadeghi, S. A. Ghasemi, B. Schaefer, S. Mohr, M. A. Lill, and S. Goedecker, The Journal of chemical physics **139**, 184118 (2013).
- ²⁴ G. Ferré, J.-B. Maillet, and G. Stoltz, The Journal of chemical physics **143**, 104114 (2015).
- ²⁵ J. Behler, The Journal of chemical physics **145**, 170901 (2016).
- ²⁶ S. De, A. P. Bartók, G. Csányi, and M. Ceriotti, Physical Chemistry Chemical Physics **18**, 13754 (2016).
- ²⁷ M. Griffiths, S. P. Niblett, and D. J. Wales, Journal of chemical theory and computation **13**, 4914 (2017).
- ²⁸ B. Temelso, J. M. Mabey, T. Kubota, N. Appiah-Padi, and G. C. Shields, Journal of chemical information and modeling **57**, 1045 (2017).
- ²⁹ G. Imbalzano, A. Anelli, D. Giofré, S. Klees, J. Behler, and M. Ceriotti, The Journal of Chemical Physics **148**, 241730 (2018).
- ³⁰ F. Musil, S. De, J. Yang, J. E. Campbell, G. M. Day, and M. Ceriotti, Chemical Science (2018).
- ³¹ W. Rudin (1976) Chap. 2, pp. 30–36.
- ³² H. W. Kuhn, Naval Research Logistics (NRL) **2**, 83 (1955).
- ³³ B. K. Horn, JOSA A **4**, 629 (1987).
- ³⁴ X. Fang, C. Wang, Y. Yao, Z. Ding, and K. Ho, Physical Review B **82**, 184204 (2010).
- ³⁵ X. Fang, C.-Z. Wang, S. Hao, M. J. Kramer, Y. Yao, M. I. Mendelev, Z. Ding, R. E. Napolitano, and K.-M. Ho, Scientific reports **1**, 194 (2011).
- ³⁶ J. J. Mcauley and T. S. Caetano, Pattern recognition **45**, 563 (2012).
- ³⁷ K. M. Anstreicher, Mathematical Programming **97**, 27 (2003).

- ³⁸ J. J. McAuley, T. S. Caetano, and M. S. Barbosa, IEEE Transactions on Pattern Analysis and Machine Intelligence **30**, 2047 (2008).
- ³⁹ T. S. Caetano, T. Caelli, D. Schuurmans, and D. A. C. Barone, IEEE Transactions on Pattern Analysis and Machine Intelligence **28**, 1646 (2006).
- ⁴⁰ D. Thain, T. Tannenbaum, and M. Livny, Concurrency and computation: practice and experience **17**, 323 (2005).
- ⁴¹ J. Han, V. Vitek, and D. J. Srolovitz, Acta Materialia **133**, 186 (2017).
- ⁴² S. Patala, Acta Crystallographica Section A: Foundations and Advances **73**, 85 (2017).
- ⁴³ H. Sheng, W. Luo, F. Alamgir, J. Bai, and E. Ma, Nature **439**, 419 (2006).
- ⁴⁴ J. Ding, Y.-Q. Cheng, H. Sheng, and E. Ma, Physical Review B **85**, 060201 (2012).
- ⁴⁵ Y.-Q. Cheng and E. Ma, Progress in Materials Science **56**, 379 (2011).
- ⁴⁶ Y. Q. Cheng, E. Ma, and H. W. Sheng, Physical Review Letters **102**, 245501 (2009).
- ⁴⁷ X. Fang, C. Wang, S. Hao, M. Kramer, Y. Yao, M. Mendelev, Z. Ding, R. Napolitano, and K. Ho, Scientific Reports **1**, 194 (2011).
- ⁴⁸ D. J. Wales, J. P. Doye, M. A. Miller, P. N. Mortenson, and T. R. Walsh, Advances in Chemical Physics **115**, 1 (2000).
- ⁴⁹ D. J. Wales, International Reviews in Physical Chemistry **25**, 237 (2006).
- ⁵⁰ M. Sonka, V. Hlavac, and R. Boyle, “Image processing, analysis, and machine vision,” (2014).
- ⁵¹ M. Comin, C. Guerra, and F. Dellaert, Journal of Computational Biology **16**, 1577 (2009).
- ⁵² D. Padhorny, A. Kazennov, B. S. Zerbe, K. A. Porter, B. Xia, S. E. Mottarella, Y. Kholodov, D. W. Ritchie, S. Vajda, and D. Kozakov, Proceedings of the National Academy of Sciences **113**, E4286 (2016).
- ⁵³ A. P. Sutton and R. W. Balluffi, *Interfaces in crystalline materials* (Clarendon Press, 1995).
- ⁵⁴ S. Patala, J. K. Mason, and C. A. Schuh, Progress in Materials Science **57**, 1383 (2012).
- ⁵⁵ S. Patala and C. A. Schuh, Philosophical Magazine **93**, 524 (2013).
- ⁵⁶ E. R. Homer, S. Patala, and J. L. Priedeman, Scientific reports **5** (2015).
- ⁵⁷ G. H. Bishop and B. Chalmers, Scripta Metallurgica **2**, 133 (1968).
- ⁵⁸ A. Sutton and V. Vitek, Philosophical Transactions of the Royal Society of London. Series A, Mathematical and Physical Sciences **309**, 1 (1983).
- ⁵⁹ A. Sutton and V. Vitek, Philosophical Transactions of the Royal Society of London. Series A, Mathematical and Physical Sciences **309**, 37 (1983).

- ⁶⁰ M. Ashby, F. Spaepen, and S. Williams, *Acta Metallurgica* **26**, 1647 (1978).
- ⁶¹ V. V. Bulatov, B. W. Reed, and M. Kumar, *Acta Materialia* **65**, 161 (2014).
- ⁶² R. Balluffi and A. Brokman, *Simple structural unit model for core-dependent properties of symmetrical tilt boundaries*, Tech. Rep. 8 (1983).
- ⁶³ This polyhedron is more precisely referred to as the Edge-Contracted-Icosahedron (ECI)⁸². In chemistry, however, the ECI is most commonly called the octadecahedron, for 18 triangular faces.
- ⁶⁴ J. L. Priedeman, C. W. Rosenbrock, O. K. Johnson, and E. R. Homer, *Acta Materialia* **161**, 431 (2018).
- ⁶⁵ R. Balluffi and A. Sutton, in *Materials Science Forum*, Vol. 207 (Trans Tech Publ, 1996) pp. 1–12.
- ⁶⁶ K. Laws, D. Miracle, and M. Ferry, *Nature communications* **6** (2015).
- ⁶⁷ X. Fang, C. Wang, Y. Yao, Z. Ding, and K. Ho, *Physical Review B* **82**, 184204 (2018).
- ⁶⁸ S. Plimpton, *Journal of Computational Physics* **117**, 1 (1995).
- ⁶⁹ Q. Wang, J. H. Li, J. B. Liu, and B. X. Liu, *RSC Advances* **5**, 46861 (2015).
- ⁷⁰ Y. Sun, F. Zhang, Z. Ye, Y. Zhang, X. Fang, Z. Ding, C.-Z. Wang, M. I. Mendelev, R. T. Ott, M. J. Kramer, and K.-M. Ho, *Scientific Reports* **6**, 23734 (2016).
- ⁷¹ S. Y. Wang, C. Z. Wang, M. Z. Li, L. Huang, R. T. Ott, M. J. Kramer, D. J. Sordellet, and K. M. Ho, *Physical Review B* **78**, 184204 (2008).
- ⁷² G. Guo, L. Yang, and S. Wu, *Intermetallics* **71**, 24 (2016).
- ⁷³ H. L. Peng, M. Z. Li, and W. H. Wang, *Physical Review Letters* **106**, 135503 (2011).
- ⁷⁴ Y. Q. Cheng, H. W. Sheng, and E. Ma, *Physical Review B* **78**, 014207 (2008).
- ⁷⁵ N. Jakse and A. Pasturel, *Applied Physics Letters* **93**, 113104 (2008).
- ⁷⁶ W.-Z. Zhang, Z.-P. Sun, J.-Y. Zhang, Z.-Z. Shi, and H. Shi, *Journal of Materials Science* **52**, 4253 (2017).
- ⁷⁷ P. H. Gaskell, *Journal of Non-Crystalline Solids* **32**, 207 (1979).
- ⁷⁸ R. Ferrando, J. Jellinek, and R. L. Johnston, *Chemical reviews* **108**, 845 (2008).
- ⁷⁹ J. Schön and M. Jansen, *Zeitschrift für Kristallographie-Crystalline Materials* **216**, 307 (2001).
- ⁸⁰ J. Schön and M. Jansen, *Zeitschrift für Kristallographie/International journal for structural, physical, and chemical aspects of crystalline materials* **216**, 361 (2001).

- ⁸¹ J. Yang, H. Li, D. Campbell, and Y. Jia, IEEE Transactions on Pattern Analysis and Machine Intelligence **38**, 2241 (2016).
- ⁸² Edge-contracted icosahedron, “Edge-contracted icosahedron — Wikipedia, the free encyclopedia,” (2017), [Online; This page was last edited on 7 June 2017, at 16:12 (UTC).].

Supplemental Materials: Point-Pattern Matching Technique for Local Structural Analysis in Condensed Matter

S1. POLYHEDRAL UNITS IDENTIFIED IN VICINAL GBS USING THE PPM ALGORITHM

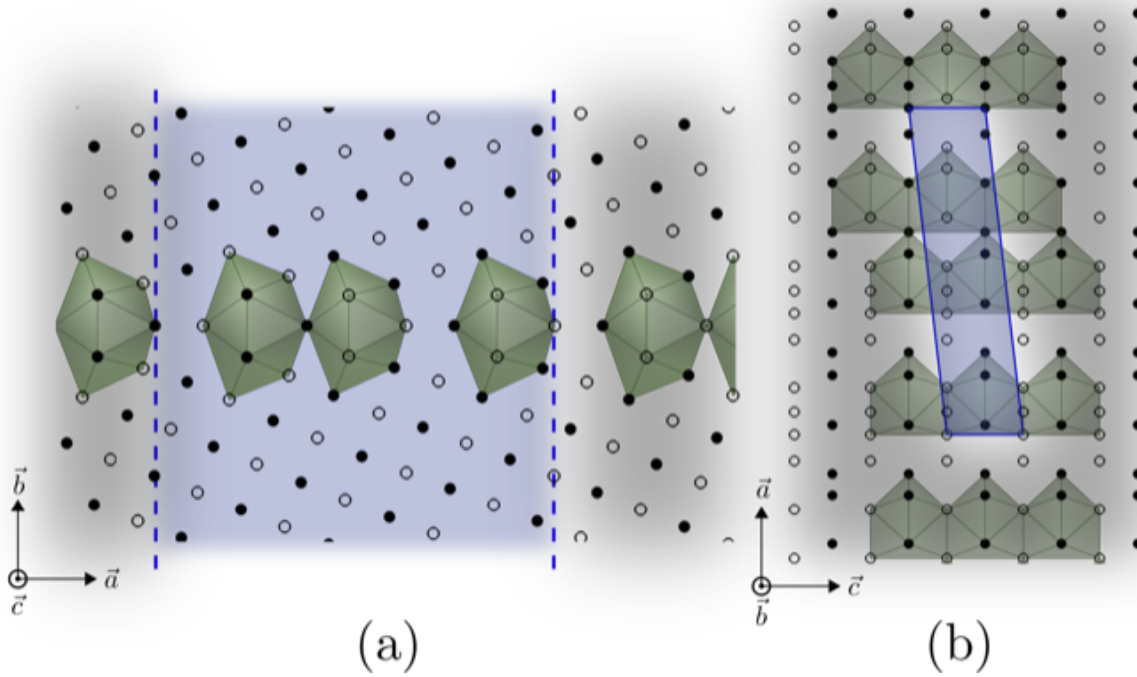


FIG. S1. The atomistic structure of $\Sigma 73$ ($0\bar{3}8$) GB is shown. The views in (a) and (b) are along the tilt axis and boundary-plane normal, respectively. The axes in the figure, \vec{a} , \vec{b} and \vec{c} correspond to the $[083]$, $[0\bar{3}8]$ and $[100]$ lattice directions, respectively.

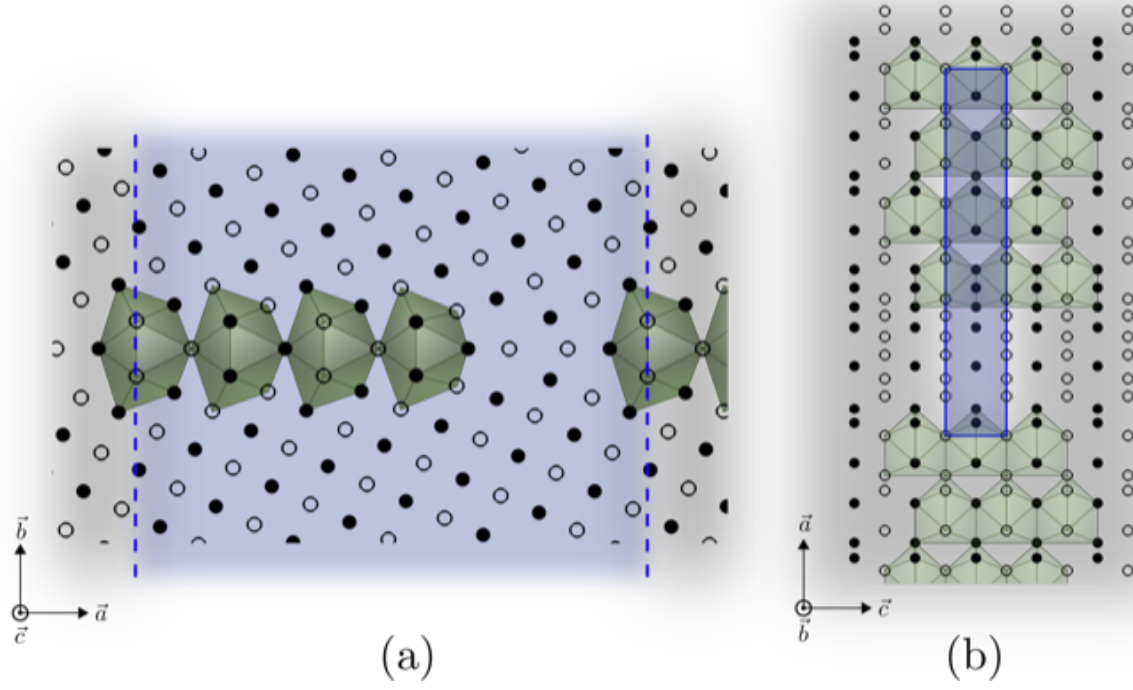


FIG. S2. The atomistic structure of $\Sigma 73(0 \bar{1} 1 5)$ GB is shown. The views in (a) and (b) are along the tilt axis and boundary-plane normal, respectively. The axes in the figure are such that, $\vec{a} = [0 \bar{5} \bar{1} 1]$, $\vec{b} = [0 \bar{1} 1 5]$ and $\vec{c} = [\bar{1} 0 0]$.

S2. STRUCTURAL UNIT MODEL FOR THE $[100]$ SYMMETRIC TILT GBS

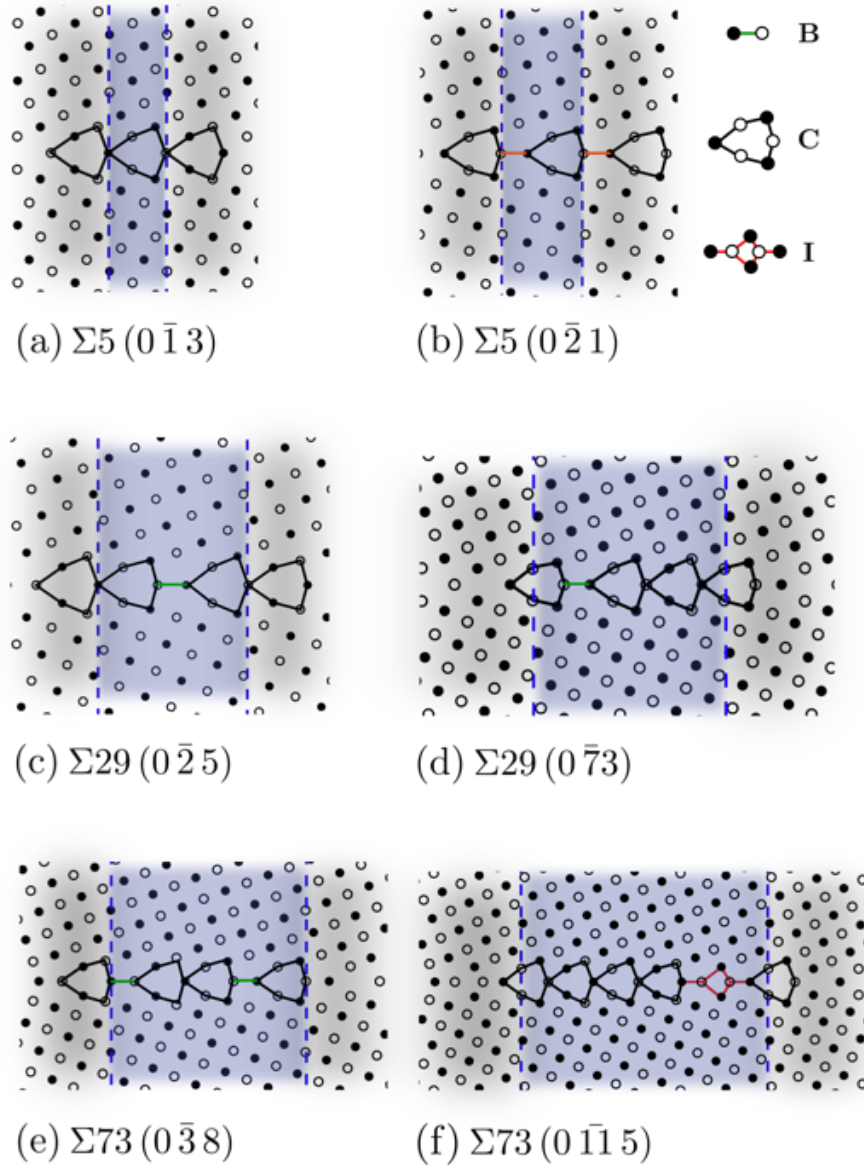


FIG. S3. The Structural Unit Model representations of all the GBs analyzed in this article are shown.